MULTI-WAVELENGTH LASER IRRADIATION OF Be-C-W COATINGS

L. AVOTINA[a,b,c], A. MARCU[b*], C. POROSNICU[b], M. LUNGU[b,c], A. STANCALIE[b], A. G. ILIE[b], P. C. GANEA[d], D. SAVASTRU[e], J. KALNACS[f], C. P. LUNGU[b], G. KIZANE[a], S. ANTOHE[c,g]

[a]*Institute of Chemical Physics, University of Latvia, Jelgavas Str. 1, LV 1004, Riga*
[b]*National Institute for Laser, Plasma and Radiation Physics, 077125 Bucharest, Romania,*
[c]*University of Bucharest, Faculty of Physics, Atomistilor Str. 405, 077125, Magurele, Romania,*
[d]*National Institute of Materials Physics Atomistilor Str. 105 bis, 077125, Magurele, Romania,*
[e]*National R&D Institute for Optoelectronics – INOE 2000, 077125 Bucharest, Romania,*
[f]*Institute of Physical Energetics, 21 Aizkraukles Str. 21, LV 1006, Riga, Latvia,*
[g]*Academy of Romanian Scientists, Splaiul Independentei 54, 050094, Bucharest, Romania.*

BeCW (3:2:1) amorphous films were irradiated with three laser wavelengths of 300, 550 and 1350 nm having a comparable energy and respectively power density. Ablated volume and preferential ablation of lighter elements seemed independent of the photon's energy, but rather on their number. Carbon and Be clustering and crystal formation into the amorphous coating were more effective with more energetic photons. Graphite structures formation was recorded for fluencies below the ablation threshold. For longer laser wavelengths, carbon atoms tend to organize in ring structures and fullerene formation was recorded around the ablation zones. Be crystals formed in the ablation zone vicinity tend to be stretched toward the film surface and toward the ablation center suggesting more defects into the formed structures for these zones.

(Received December 17, 2015; Accepted March 24, 2016)

Keywords: Laser-matter interaction, Carbon structures, Be crystal

1. Introduction

Fusion reaction between tritium and deuterium is among perspective ways of producing energy. By achieving Lawson criterions [1], fusion reactions are possible in magnetic confinement devices, like tokamak [2] type devices. A number of technologies and materials are tested in tokamak type reactor to be constructed: International Experimental Reactor (ITER) for the development of the demonstration power plant (DEMO) [2]. Presently the largest tokamak type device, where materials are tested for ITER and DEMO, is Joint European Torus (JET). Since for ITER the plasma facing materials to be used will be tungsten (W) in the divertor area and beryllium (Be) for the inner first wall, from 2011 in JET operates with ITER like wall (ILW) [3], where plasma facing surfaces are in the same distribution as it is planned for ITER. The first wall zone is from beryllium, while divertor consist from tungsten coated carbon fiber composite (CFC) tiles and bulk tungsten tiles [4,5].
Due to plasma interactions with the walls caused by imperfect confinement as well as instabilities in the fusion plasma (disruptions, ELM's, etc.) during plasma operation sputtering of the PFC surface may occur, followed by transport in plasma and redeposition in remote areas. Interactions on divertor surface forms a deposited layer [6], where retention of fusion fuel is possible. The deposited layer contains plasma facing wall elements as well as carbon from the CFC as impurities [6]. The presence of the deposited layer can influence the properties of the inner wall as well as the thermal conductivity of the divertor materials. Also, during plasma disruptions, the PFC are subject to high heat fluxes. Therefore, it is important to expand the knowledge about high fluence interactions with deposited layers.

*Corresponding author: aurelian.marcu@inflpr.ro

Such interaction are generally depending not only on the plasma energy but also on the type of the particles and photons energy interacting with the walls. Thus, since in the tokamak there are different types of radiation [7-9], the wall damage would also depend on the irradiation spectra. The high-energy fusion plasma wall interaction (PWI) can be simulated by laser irradiation [10], and it could also modify the materials structures even below the ablation threshold [11-17]. In this paper, we investigate wavelength dependent effects of laser irradiation on the BeCW amorphous coatings.

2. Experimental system and techniques

The BeCW coating on Si substrate was deposited using Thermionic vacuum arc (TVA) technique. TVA technique is a suitable method for deposition of mixed layers similar to those predicted to appear during fusion plasma operation, qualitatively comparable with fusion technology [13]. TVA involves steady DC discharges that ignites under high vacuum conditions in the vapors of the interest material [18]. Exact atomic ratios of the coating are 50%; 33% and 17% for Be, C and W, respectively. Film thickness was about 100 nm.

Coating irradiation was performed with a Continuum FX-1 Sunlite Nd:YAG tunable laser, having the pulse length 7 ns and using the burst mode. It was used a 17.7±1.7 mJ energy/pulse for three different wavelengths 300, 550 and 1350 nm, representing ultraviolet, visible and infrared radiation, respectively. A generic experimental scheme of the experimental system is presented in Fig. 1.

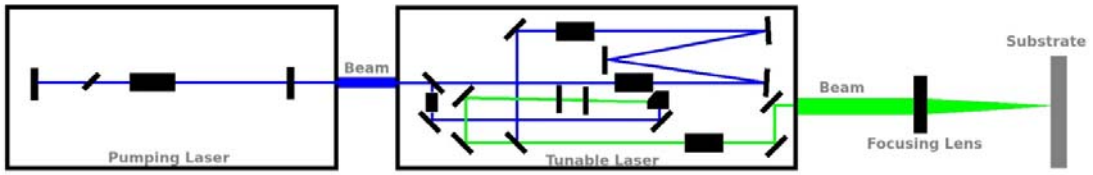

Fig.1. Experimental system

One pulse ablated area can roughly be approximated as circular with energy distribution over the irradiated zone described by a Gaussian function in the form of:

$$f(x) = \frac{E_n}{\sigma_x \sqrt{2\pi}} e^{-\frac{(x-\mu_x)^2}{2\sigma_x^2}} \tag{1}$$

where: E_n is the spot energy, μ_x and σ_x are spot center position and respectively dispersion on the axis (approximated with pulse width/6).

Morphology investigation were made by a Scanning Electron Microscopy (SEM) using a 'FEI–INSPECT S' microscope. Raman spectra were recorded using Jasco Raman spectrometer with 532 nm Nd:YAG laser, 633 nm HeNe and 785 nm diode laser. In our experiment, Raman laser parameters for mapping were, λ= 532 nm, exposure time: 30s, accumulations: 3, objective: 20x, resolution: 10 cm^{-1} and laser power 3mW.

In a hexagonal graphite single crystal structure correspond to the D_{6h}^4 (=$P6_3/mmc$) space group [19]. The Raman active mode in graphite (G-peak) at 1581 cm^{-1} has E_{2g} symmetry [19]. In the highly oriented graphite, nanocrystalline graphite and glassy carbon the G-peak does not disperse, (does not change the position with excitation wavelength). With increase of disorder the dispersion of G-peak increases, the position of G-peak increases as excitation energy increases [20]. Dispersion of Raman modes is characteristic for the disorder related (D-peak) in polycrystalline graphite as well [21]. Similar as for the G-peak, position of D-peak increases as increases excitation energy. For excitation energy 1.5 eV the position of D-peak is closing to 1300 cm^{-1}, while for excitation energy around 3 eV D-peak position reaches 1380 cm^{-1} [22]. For characterization of various carbon materials (disordered graphite, diamond-like carbon materials)

another feature from Raman spectra is widely used – the intensity ratio between D- and G-peak (I_D/I_G) [23-26]. Tuinstra and Koenig noted that I_D/I_G varies inversely with graphite crystallite size L_a [19, 21]. As well as an increase of I_D/I_G correspond to increasing disorder of graphite. In case if L_a is below 2 nm, the Tuinstra and Koenig relation is not valid and L_a is proportional to square root of I_D/I_G [18].

For the metals, the surface plasmons limit the penetration of light and therefore the Raman signal usually is extremely weak [27]. However, beryllium with a hexagonal close packed structure is an exception. The hexagonal close packed (hcp) structure allows one Raman-active phonon mode in single crystal 463 cm^1. The only Raman active mode of the space group of Be lattice D_{6h}^4 is E_{2g} [28]. In polycrystalline beryllium the signals are observed at 455 cm^{-1} (514 nm) [29] and 457 cm^{-1} (488 nm) [30, 31].

Raman spectra were measured using three different wavelengths – 532, 633 and 785 nm. From Beer-Lambert law with increasing wavelength it also increases the penetration depth. For carbon the penetration depth of 532 nm is around 50 nm and for 633 nm - ~70 nm. Respectively with 633 and 785 nm laser additional information about deeper layers of the BeCW coating can be obtained. However, in Raman spectra measured with 532 and 633 nm beryllium signal is quite intensive and narrow, in Raman spectra measured with 785 nm the signal/noise ratio being too low to distinguish a beryllium signal.

FT-IR spectroscopy measurements were performed with a Perkin Elmer Spotlight 400 FT-IR apparatus. The measurements were made in reflection mode with accumulations: 20, aperture 10, objective: 20x, resolution: 2 cm^{-1} and recorded spectra between 450 and 1500 cm^{-1}.

3. Results and discussions

During laser irradiation in the central part of the ablated areas, the coating is partially or completely removed and silicon substrate is uncovered and even damaged. Electron microscopy images of the irradiated surfaces are presented in the Fig. 2. As could be seen in the inset presenting the center of the ablation zones, after irradiation with 300 nm, in the central part the coating is removed and the substrate and the damaged Si surface is rather rough. For the 550 nm pulse, the central part of irradiated spot is also affected, but, as can be seen in inset of the Fig.2, the surface is more smooth than for 300 nm pulse, while the spot size is larger. After 1350 nm irradiation, the spot trace is increased in comparison with 300 and 550 nm zones. The surface modification seems to be less intense than for visible and UV pulses. Unlike for the other two wavelengths, some structures seems to be present in central part of irradiated spot, as can be seen in inset of 1350 nm irradiated spot area.

Further from the central part and exfoliation of BeCW coating from Si, where the substrate was less affected by the laser pulse, a change in the coating color is visible around all spots, but without significant changes in the morphology, suggesting the presence of structural modification for these zones.

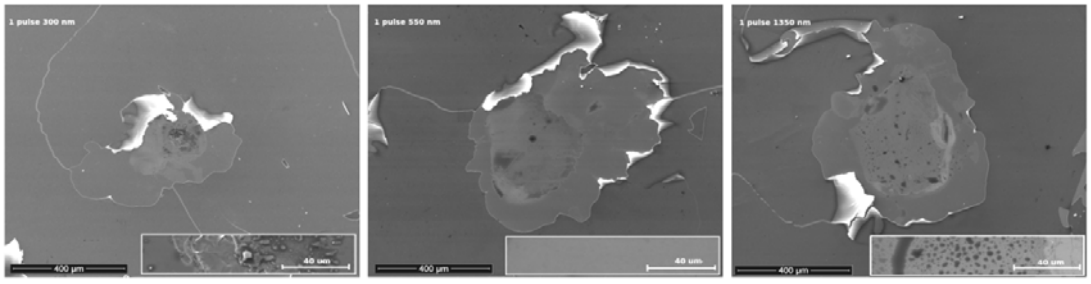

Fig. 2. SEM images of irradiated spot areas 300, 550 and 1350 nm

The elemental composition in the irradiated areas were analyzed by energy dispersion X-ray spectroscopy (EDX) and comparative results for the three film constituents over the three spots are presented in Fig. 3.

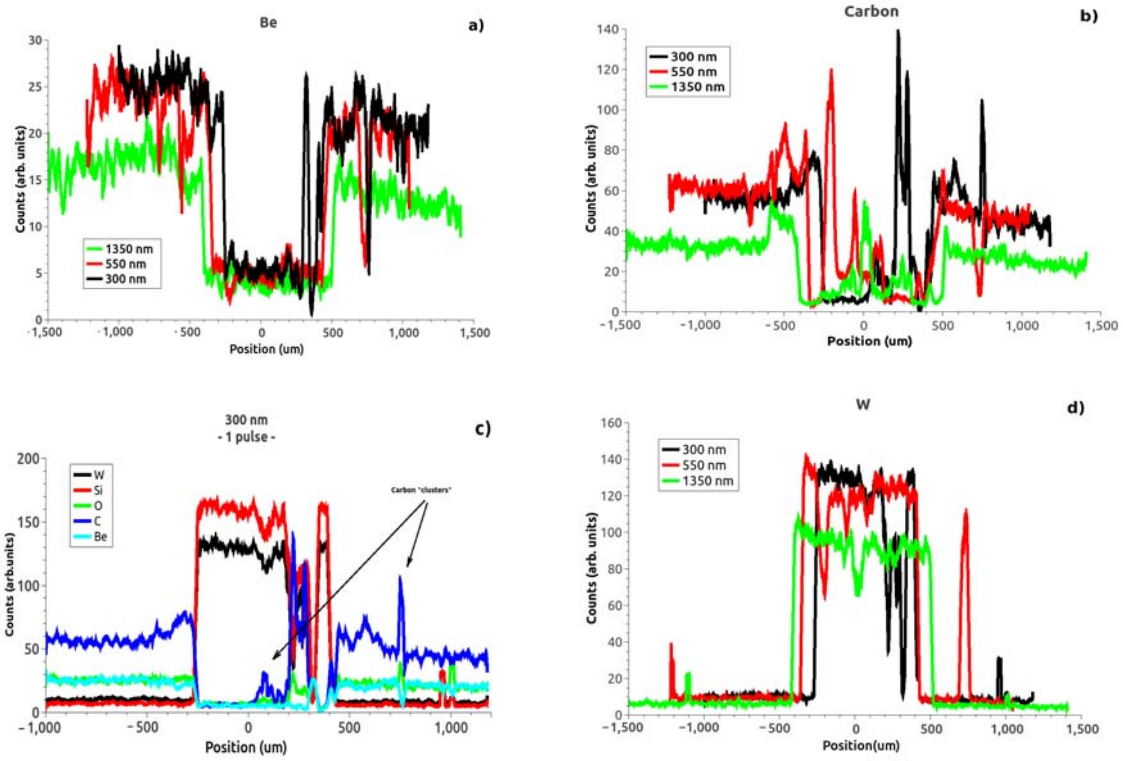

Fig. 3 EDX analysis of element distribution on the ablation spots for: a) beryllium, b) carbon, c) Be, C and W variation over the 300 nm irradiation spot and d) element distribution on the ablation spots for tungsten

As visible in Fig. 3a in the central part of irradiated areas the amount of beryllium is decreased. The EDX results confirm the SEM results regarding dependence of the size of the ablated areas on the laser wavelength. The strongly affected area is having a smaller diameter for the shorter irradiation wavelengths. As can be seen in Fig.3a, for 300 nm spot close to edge of ablated area and around it, appear some sharp changes in the recorded amount of beryllium. For longer wavelengths, respectively for 1350 nm pulse spot, the change in Be amount is less sharp than for 300 and 550 nm spots.

Carbon ablation after irradiation with 3 different wavelengths is inhomogeneous. In all three cases amount of carbon is decreasing towards central part of irradiated area. However, in all cases a slight increase on edges of the ablated area and few peaks in the central zones are visible (Fig. 3b). The agglomeration effect in the central part and on the edges of the central part seems to be more intense for 300 nm pulse spot than for other wavelengths. However, for the 1350 nm spot, the amount of carbon even increases somewhere in the middle of the irradiated spot, supporting a diffusion or re-deposition process.

It should be further emphasized that carbon distribution is in most of the zones, comparable but less uniform with the beryllium distribution. While comparing the Be and C distribution for the 300 nm irradiated zone (Fig. 3c) the peaks are mostly fluctuating together. However, the carbon increase near the ablation zone edges and two more individual peaks marked on the image do not have a correspondent in the Be peaks. In one case it even corresponds to a decrease of the Be. Thus, we can not talk about a 'preferential' ablation of the carbon in some zones but rather about a carbon cluster formation through re-deposition or diffusion processes, that takes place in these zones. The presence of such clustering in the presence of high temperature generated by the photonic interaction suggest possible formation of C and Be structures in these zones.

In contrast to Be and C behavior, relative amount of tungsten in the central part of ablated areas is higher than in non-ablated parts (Fig.3d). Since the W concentration is about 1/6 in the initial coating, the increased amount of tungsten in the central parts of the irradiated spots shows preferential ablation of beryllium and carbon in comparison with tungsten, while the slight decrease in amount of tungsten in some

points of the central parts of the spot are correlated with the inhomogeneous distribution of carbon in those zones.

By using both SEM and EDX results and approximating the energy distribution on a beam diagonal with the formula (1) we were estimating the ablation threshold for the three laser wavelengths. In the case of the SEM images we mediated the diameter of the ablation on the spot diagonal on several direction, while from the EDX data were measured the distances between the sharp edges of the C and Be spatial variations. The obtained results are presented in Fig 4, together with an averaged curve for all obtained results. Furthermore, by considering the beam's energy in the form of:

$$E = n*h*\nu \tag{2}$$

where, E is the pulse spot energy, n is the total number of photons in the beam, h is Plank constant and ν is the photon frequency and respectively:

$$\gamma = \frac{1}{\lambda} \tag{3}$$

with λ laser wavelength, we obtain for the three laser wavelengths (with about same energy of about 17mJ) a different number of photons per beam spot in the form of:

$$n = \frac{E\lambda}{h} \tag{4}$$

If we roughly estimate the number of atoms in film and divide the number of photons per number of atoms in the film volume, we obtain the dependence of the ablation threshold (in this case for a complete 100 nm film removal) on the incident number of photons per atom presented in the inset of the Fig. 4.

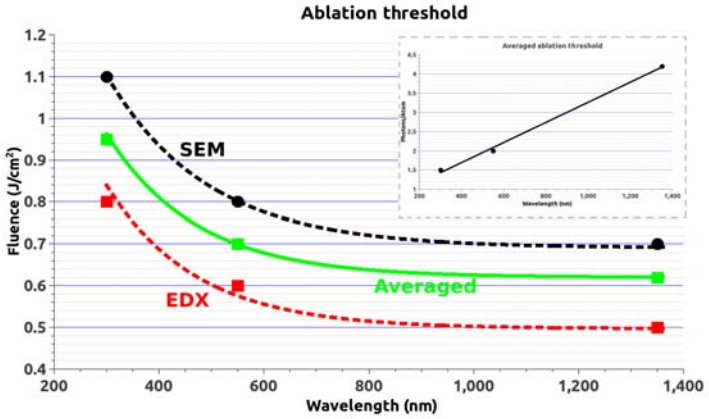

Fig. 4 Ablation threshold (for a 100 nm film removal) dependence on the laser wavelength, estimated from SEM and EDX results. Inset: threshold number of photons/atoms as a function of laser wavelength.

As could be seen, the efficiency of the photons is quazi-linearly decreasing with the photon energy for the given film thickness of about 100 nm. However, since the material is extracted from a smaller area for shorter beam wavelength we could conclude that overall, the more energetic photons are depositing more energy out of the beam into the substrate. Thus, it should be natural to expect more structural modifications for shorter radiation wavelengths induced the injected energy.

Spot trace of the 300 nm beam, was investigated by Raman spectroscopy using a 532 nm Raman laser wavelength on a 2D matrix points presented in Fig.5a. Thus, Raman measurements were performed with a 40 μm step, covering an area of 640x440 μm. A highlighted area in optical microscope image

corresponds to the uncovered Si substrate. From each Raman spectrum the intensity of Be peak of a E_{2g} mode was obtained and the be peak intensity values were plotted accordingly to the previously settled matrix in Fig.5b. We noticed, that the Be peak intensity variation shows significant similarities with the optical image. Peak intensity decreases towards the central part of ablated area. However, some signs of Be presence can be seen in zones, where substrate is highly modified (ablated), as well. That shows some Be migration or re-deposition processes in the areas with a higher surface roughness.

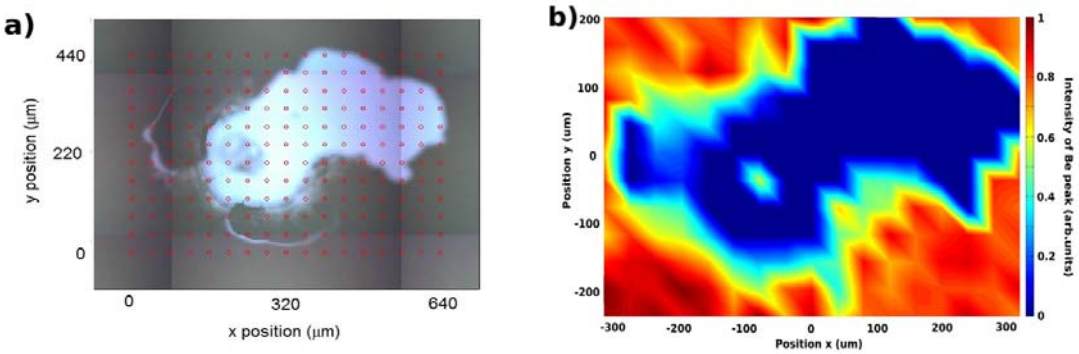

Fig. 5. a) Optical image of 300 nm irradiated spot area with a matrix for Raman mapping, b) Be peak intensity from Raman spectra

While examining the Be peak position in Raman spectra, we noticed that Raman shift of Be peak decreases towards the center of irradiated spot. A Be peak Raman shift map is represented in Fig. 6a. Around the ablated zone, Be peak Raman shift value is as low as 441 cm^{-1}. With increasing the distance from ablated are Be peak value increases up to 447-449 cm^{-1}.

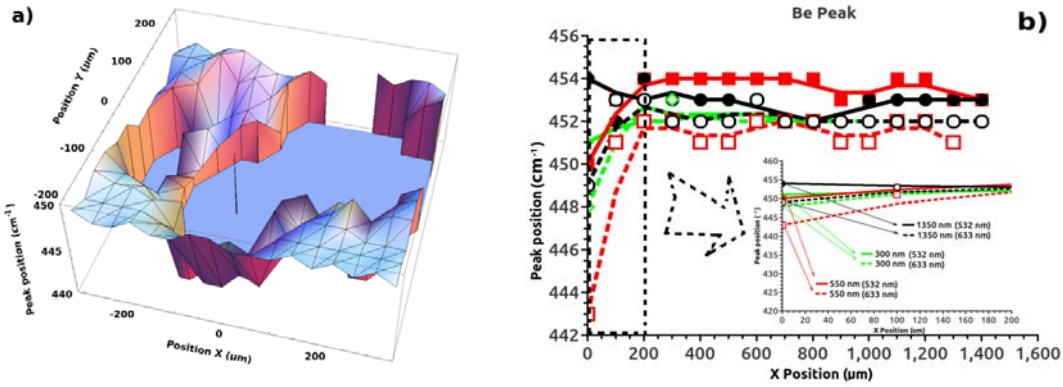

Fig.6. Be peak position in Raman spectra a) around edges of ablated spot, b) from the edge of ablated area

Raman measurements with a step of 100 µm were further extended from the ablated zone edge. In order to obtain in depth information of Be structure, two different Raman laser wavelengths were used – 532 and 633. The obtained results are represented in Fig.6b. It can be seen that on the edge of ablated area Be peak Raman value is lower than at larger distances from the ablated zone. We emphasize a tendency of more decreased Be peak value with a shorter Raman laser wavelength. That shows a higher influence of the irradiation on the superficial layers. Nevertheless, a slight trend in decreasing of Be peak position with the decrease of irradiation laser wavelength is visible in inset of Fig.6b. This shows that shorter irradiation wavelength produces more distorted Be crystals. One possibility would be a higher transferred energy to the non-ablated material generating more diffused material (e.g. carbon) or Be bonds (e.g. BeO, since the irradiation was performed in air)

In the Raman spectra mapping, carbon related peaks were observed as well. Around 1500 cm^{-1} was observed a peak, assigned as graphite G-peak, present in graphitic and disordered carbon materials. G-peak arises in the same mode as in Be structure, E_{2g} mode vibrations. The size of the graphite crystallites is estimated to about 1.6 nm (+/- 0.4 nm) with no particular trend variation. (However we should mention that the due to the noise spectra, reasonable estimation could be made only for deeper layers by using the 785 nm Raman laser wavelength.) The variation of full width in half maximum ($FWHM_G$) of this peak is shown in Fig.7a. G-peak is hardly visible in the central part of irradiated spot in spite of the carbon presence shown in the EDX measurement. This suggest that in the central area, agglomerated carbon is hardly forming crystals. Towards the edges of the ablated zone, a decrease in $FWHM_G$ occurs. At larger distances from the edge of ablated area was investigated with different Raman laser wavelengths as well.

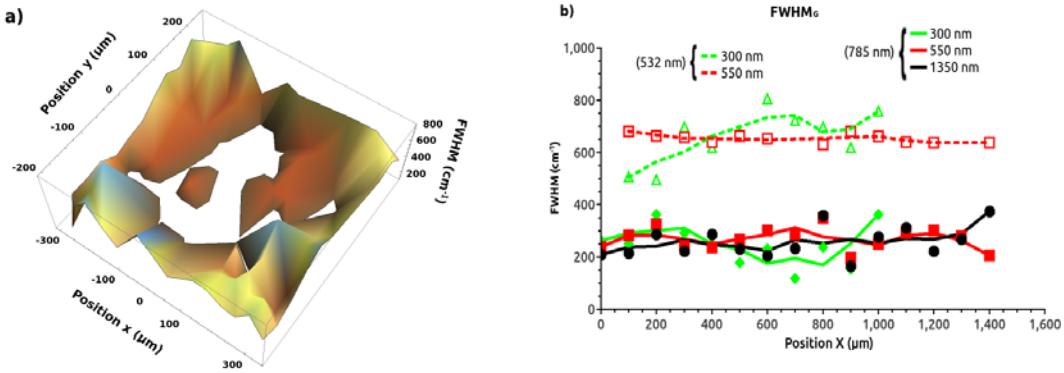

Fig.7. Full width in half maximum of G-peak
a) around edges of ablated spot, b) from the edge of ablated area

As seen in the image 7b) there is decreasing trend toward the ablation zone only for the 300 nm spot and only on the surface. All other curves present no clear trend in spatial variation of the FWHM of the G-peak. However, closer to the surface (analyzing with 532 nm), G-peak is very broad (Fig.7b) comparing with deeper layers. Such information was obtained by infrared, 785 nm Raman laser. Thus, it seems that the carbon tend to form graphite structures in the vicinity of the ablation zone, but, on the surface they tend to have defects. Somehow, more energetic photons manage to prevent that even on the surface but only in the ablated zone close vicinity.

FT-IR investigations were made in order to analyze the chemical composition of the irradiated surfaces. Main FT-IR results are represented in Fig.8.

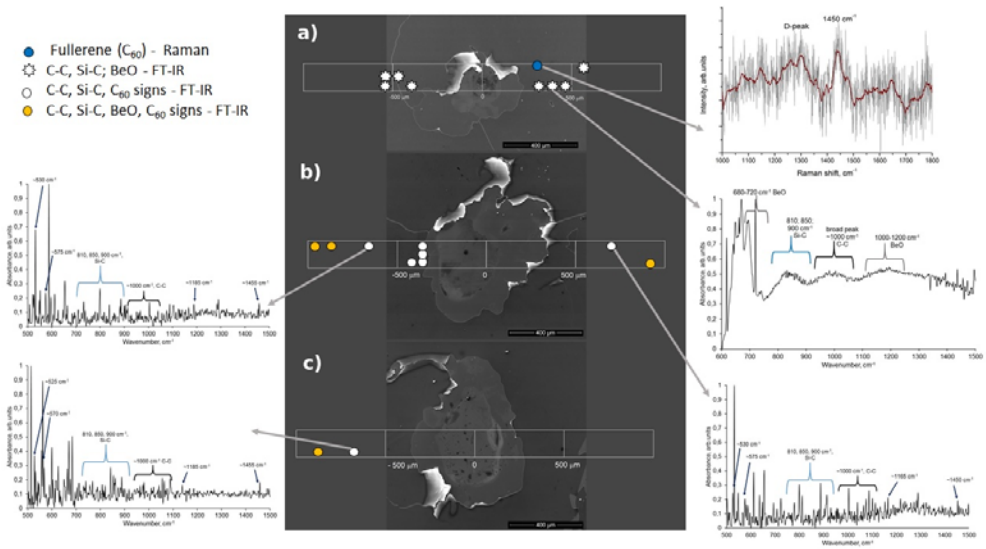

Fig.8. SEM images of 300, 550 and 1350 nm irradiated areas with points where specific structure's spectra were observed

A broad peak 900-1000 cm^{-1} correspond to C=C sp^2 deformation vibrations [32] (Fig.8) and they are tend to be present for 550 nm irradiation wavelengths from the edge of the ablation zone, while for the 1350 nm only further from the central zone. Peaks at 810, 850 and 900 cm^{-1} show to presence of SiC [33] and they tend to be present in all the spectra. They suggest a reaction between the carbon and the substrate. Signals in range 1000-1200 cm^{-1} approve the presence of BeO [34] in the ablation zone periphery. As also seen in the Fig.8, by FT-IR mapping, fullerene C_{60} peaks were observed in the vicinity of the 550 nm irradiated area and at bigger distances for 1350 nm irradiation area, while for the 300 nm there were only some possible signals from the Raman investigations. It should be mentioned that the small Raman peak could also be attributed to this structure since a peak ~1450cm^{-1} could correspond to a shifted fullerene C_{60} peak [35, 36]. Thus, for this laser irradiation wavelength, the presence of the fullerene is also very probably among the other formed structures.

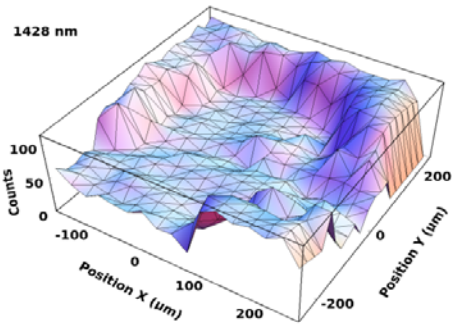

Fig. 9. 1428 cm^{-1} peak reflection mapping for 300 nm laser wavelength trace on the BeCW film

By FT-IR mapping for the 1430 cm^{-1}, (that corresponds to C-C stretch in ring [37]) the data presented in Fig. 9 were obtained. Thus, after laser irradiation, carbon atoms tend to organize in ring like structures, leading to graphitization but also possible formation of spherical structures as fullerene-like particles.

4. Conclusions

While irradiating beryllium-carbon-tungsten coatings with different wavelengths, the ablation efficiency depends on number of photons rather than their energy, and higher energetic photons will mainly deposit more energy into the coating enhancing structural modification as observed for 300 nm beam in comparison with the 1350 nm one. In the mixture of beryllium-carbon and tungsten a preferential ablation of beryllium in comparison to other elements takes place. The less affected element by laser irradiation is tungsten.

In the ablation zone vicinity, irradiated below the ablation threshold, through the injected energy and carbon diffusion, Be and C structures are formed. After laser irradiation, carbon atoms tend to organize in ring structures, but fullerene structures are mostly present for the more energetic photons of 300 nm. Present in the ablation zone periphery for all irradiation wavelengths are graphite (distorted) structures. In general, all the structures are more distorted closer to the surface than in depth. Be forms metallic structure and BeO could be seen in the ablation zone periphery but also for more energetic photons of 300 nm.

Acknowledgements

This work was supported by a grant of the Romanian National Authority for Scientific Research, CNCS – UEFISCDI, project number PN-II-IDPCE- 2011-3-0522 and Ministry of Science and Education of Latvia. A. Stancalie acknowledges the financial support of the Romanian National Authority for Scientific Research - ANCS, project number LAPLAS 3, cod PN 09 39. The procurement of the Continuum FX-1 Sunlite Nd:YAG tunable laser was financially supported by UEFISCDI, grant 8PM/2010. Authors thank to N.I.M.P. for the access to Perkin Elmer Spotlight 400 FT-IR apparatus.

References

[1] D.J. Lawson, Proceedings of the Physical Society, Section B, Volume 70, Number 1, 1957
[2] G. Federici, C.H. Skinner, J.N. Brooks, J.P. Coad, C. Grisolia A.A. , Haasz, A. Hassanein, V. Philipps, C.S. Pitcher, J. Roth, W.R. Wampler, D.G. Whyte, Nuclear Fusion, **41**(12R), 1967 (2001)
[3] E. Joffrin, M. Baruzzo, M. Beurskens, C. Bourdelle, S. Brezinsek, J. Bucalossi, Buratti P., G. Calabro, Challis C.D., Clever M., Coenen J., Delabie E., Dux R., Lomas P., de la Luna E., P. de Vries, Flanagan J., Frassinetti L., Frigione D., Giroud C., Groth M., Hawkes N., J. Hobirk, Lehnen M., Maddison G., Mailloux J., Maggi C.F., Matthews G., Mayoral M., A. Meigs, Neu R., Nunes I., Puetterich T., Rimini F., Sertoli M., Sieglin B., Sips A.C.C., G. van Rooij, Nuclear Fusion **54**, 013011 (2014)
[4] J. Paméla, F. Romanelli, M.L. Watkins, A. Lioure, G. Matthews, V. Philipps, T. Jones, A. Murari, Géraud, Crisanti F., Kamendje R., Fusion Engineering and Design **82**, 590 (2007).
[5] J. Paméla, G.F. Matthews, V. Philipps, R. Kamendje, Journal of Nuclear Materials **363-365,** 1 (2007)
[6] P. Petersson, M. Rubel, H.G. Esser, J. Likonen, S. Koivuranta, A. Widdowson, Journal of Nuclear Materials, **463,** 814 (2015).
[7] D.Hh Morozov, E.O. Baronova, Senichenkov I.Yu, Plasma Physics Reports, **33(**11), 906 (2007)
[8] T.D. Buchell, J.P. Strizak, Nuclear Engineering and Design, **271,** 262 (2014).
[9] K. Yada, N. Matsui, N. Ohno, S. Kajita, S. Takamura, M. Takagi, Journal of Nuclear Materials **390-391,** 290 (2009)
[10] C.P. Lungu, C.M. Ticoş, C. Poroşnicu, I. Jepu, M. Lungu, A. Marcu, C. Luculescu, G. Gojocaru, D. Ursescu, R. Bănici, G.R. Ungureanu, Applied Physics Letters **104**, 101604 (2014)
[11] J. Yin, Zhang H., Xiong X., Huang B., Zuo J., Applied Surface Science **255,** 5036 (2009)
[12] A. Hu, Rybachuk M., Lu Q.-B., Duley W.W., Appl. Phys. Lett. **91**, 131906 (2007)
[13] M. Shinoda, Gattass R.R., Mazur E., Journal of Applied Physics **105**, 053102 (2009)

[14] C.P. Lungu, Grigorescnicu C., Lungu A.M., Feraru I.D., Savastru D., Diamond & Related Materials, **20**, 1061 (2011).
[15] M. Forster, L. Égerházi, C. Haselberger, Huber C., Kautek W., Appl Phys A **102**: 27 (2011)
[16] A. Marcu, L. Avotina, C. Porosnicu, A. Marin, C.E.A. Grigorescu, Ursescu D., Lungu M., N. Demitri, Lungu C.P., Appl. Surf. Sci. acepted **355,** 477 (2015)
[17] Q. Nian, Y. Wang, Y. Yang, J. Li, Zhang M.Y., Shao J., Tang L., Cheng G.J., Sci. Rep. **4**, 6612 (2014).
[18] C.P. Lungu, C. Porosnicu, I. Jepu, M., Lungu A. Marcu, C. Luculescu, C. Ticos, A. Marin, C.E.A. Grigorescu, Vacuum, **110**,207 (2014)
[19] F. Tuinstra, J.L. Koenig, J. Chem. Phys. **53**, 1126 (1970)
[20] A.C. Ferrari, J. Robertson, Physical Review B,.**61**, No.20, (2000)
[21] A.C. Ferrari, J. Robertson, Phil.Trans. R. Soc. Lond. A, **362**, 2477 (2004)
[22] I. Pośik, M. Hundhausen, M. Koós, L. Ley, journal of Non-Crystalline Solids **227-230,** 1083 (1998)
[23] K. Sato, R. Saito, Y. Oyama, J. Jiang, Cançado L.G., Pimenta M.A., Jorio A., Ge.G. Samsonidze, Dresselhaus G., Dresselhaus M.S., Chemical Physics Letters **427,** 117 (2006)
[24] F.C. Tai, S.C. Lee, C.H. Wei, S.L. Tyan, Materials Transactions, **47**(7), 1847 (2006)
[25] M.A. Pimenta, G. Dresselhaus, M.S. Desselhaus, L.G. Cançado, A. Jorio, R. Saito, Physical Chemistry Chemical Physics, **9**, 1276 (2007)
[26] A. Sikora, F. Garrelie, C. Donnet, A.S. Loir, Fontaine J., Sanchez-Lopez J.C., Rojas T.C., Journal of Applied Physics **108**, 113516 (2010)
[27] C. Pardanaut, C. Martin, G. Giacometti, P. Roubin, Pégourié B., Hopf C., T. Schwarz-Selinger, Jacob W., Buijnsters J.G., Diamond & Related Materials **37**, 92 (2013)
[28] G. Gouadec, P. Colomban, Progress in Crystal Growth and Characterization of Materials **53,** 1 (2007)
[29] L.M. Fraas, S.P.S. Port, E. Loh, Solid State Communications **8m,** 803 (1970)
[30] D. W. Feldman, J. H. Parker Jr. and M. Ashkin, Physical Review Letters, **21**, 607 (1968)
[31] H. Olijnyk, A.P. Jephcoat, J. Phys.: Condens. Matter **12**, 8913 (2000)
[32] C. Arnas, Dominique, Roubin P., Martin C., Brosset C., Pegurie B., Journal of Nuclear Materials **353**, 80 (2006)
[33] H. Mutschke, A.C. Andersen, D. Clement, Th. Henning, G. Peiter, Astronomy and Astrophysics, **345**(1), pp. 187
[34] J. Baima, A. Erba, M. Rerat, R. Orlando, R. Dovesi, The Journal of Physical Chemistry C, **117**(24), pp. 12864
[35] V. Schettino, M. Pagliai, L. Ciabini, G. Cardini, J.Phys.Chem A., 11192 (2001)
[36] D.L. Baptista, F.C. Zawislak, Diamond & Related Materials **13**, 1791 (2004)
[37] A.C. Ferrari, S.E. Rodil, J. Robertson, Physical Review B **67**, 155306, 1 (2003)